Elucidating the Sodiation Mechanism in Hard Carbon by Operando Raman Spectroscopy

Julia S. Weaving[1], Alvin Lim[1], Jason Millichamp[1], Tobias P. Neville[1], Daniela Ledwoch[1], Emma Kendrick[2,5], Paul F. McMillan[3], Paul R. Shearing[1,5], Christopher A. Howard[4]*, Dan J. L. Brett[1,5]*

[1]Electrochemical Innovation Laboratory, Department of Chemical Engineering, University College London, London, WC1E 7JE, UK

[2]School of Metallurgy and Materials, University of Birmingham, Birmingham, B15 2TT, UK

[3]Department of Chemistry, University College London, London, WC1H 0AJ, UK

[4]Department of Physics & Astronomy, University College London, London WC1E 6BT, UK

[5]The Faraday Institution, Quad One, Harwell Science and Innovation Campus, Didcot, OX11 0RA, UK

ABSTRACT

Operando microbeam Raman spectroscopy is used to map the changes in hard carbon during sodiation and desodiation in unprecedented detail, elucidating several important and unresolved aspects of the sodiation mechanism. On sodiation a substantial, reversible decrease in G-peak energy is observed, which corresponds directly to the sloping part of the voltage profile and we argue can only be due to steady intercalation of sodium between the turbostratic layers of the hard carbon. Corresponding reversibility of the D-peak energy change is consistent with intercalation rather than representing a permanent increase in disorder. No change in energy of the graphitic phonons occurs over the low voltage plateau, indicating that intercalation saturates before sodium clusters form in micropores in this region. At the start of the initial sodiation there is no change in G- and D-peak energy as the Solid Electrolyte Interphase (SEI) forms. After SEI formation, the background slope of the spectra increases irreversibly, due to fluorescence. The importance of *in situ*/operando experiments over *ex situ* studies is demonstrated; washing the samples or air exposure causes the G- and D-peaks to revert back to their original states owing to SEI removal and sodium de-intercalation and confirming no permanent damage to the carbon structure.

1. Introduction

Sodium-ion (Na-ion) batteries are receiving increasing attention, particularly for stationary applications, such as load-levelling, and have a number of significant benefits over lithium ion (Li-ion) batteries.[1-9] Whereas lithium is only present in limited amounts in the earth's crust and is found in local deposits, sodium is more plentiful, ubiquitously-found and has a substantially lower cost.[5-6] Additionally, an expensive copper current collector is required for the anode in Li-ion systems because lithium alloys with aluminium. This is not the case with sodium, therefore, aluminium can be used as the current collector for both electrodes, saving on cost. Moreover, because copper is not present, Na-ion cells can be discharged fully to zero volts, for safer storage and transportation since aluminium does not dissolve

2

into the electrolyte at these voltages.[7] Furthermore, the rate of self-heating is lower than for Li-ion technologies.[8-9] These considerations contribute to the promise of higher safety in Na-ion systems compared with their Li-ion counterparts. However, the Solid Electrolyte Interphase (SEI), which is a layer that forms on the surface of the carbon during the initial sodiation, resulting from the decomposition of the electrolyte at the pristine carbon surface, is reported to be primarily inorganic for Na-ion systems and less stable and more soluble compared with the Li-ion SEI, which is primarily organic.[10-12] Although the SEI in Li-ion systems is relatively well understood, further work is required to understand and improve the stability of the SEI in Na-ion systems to benefit both cycle life and safety, as it protects against further electrolyte decomposition on the carbon surface.[13-14]

Another significant challenge for Na-ion batteries is to find suitable electrode materials. The graphite electrodes incumbent in Li-ion batteries cannot be used for Na-ion anodes because sodium does not intercalate into graphite at ambient pressure.[15] On the other hand, hard carbons have emerged as suitable systems for reversibly storing Na$^+$ ions, giving capacities of up to 300 mA h g^{-1}.[16-17] Furthermore, hard carbon can be made via pyrolysis from relatively inexpensive biomass sources. Hard carbons contain regions of randomly stacked graphitic to graphene-like layers (turbostratic nanodomains - TNDs), cross-linked by amorphous regions containing sp^3-bonded sites.[18-20] The crystallinity, defect density, TND domain-size and porosity of the hard carbons can be controlled, for example, by changing the precursor or carbonization temperature.[21-24] However, the optimization of the hard-carbon microstructure for Na-ion batteries requires detailed understanding of the mechanism by which sodium inserts into the hard carbon structure. This mechanism is currently under intense debate[11, 16, 19-33] with sodium storage thought to occur via a combination of edge/defect site occupancy, intercalation and pore filling. The voltage profile upon electrochemical sodiation and desodiation of hard carbon is well known; upon sodiation it shows a characteristic linear decrease in potential over approximately 50% of the capacity, to around

3

100 mV followed by a flat region (plateau) over the remaining capacity. Diffusion coefficient measurements[21, 24] and heteroatom doping studies[29] conclude that the linear sloping region of the voltage profile (from ~1 V to ~100 mV) results from sodium occupation of edge and defect sites and the plateau below ~100 mV from sodium intercalation into the TNDs and occupation of the pores, although the apparent correlation between slope capacity and concentration of defects[21] may be better explained by the observation that samples with a higher number of defect sites also have higher surface area, and show a lower efficiency, which is consistent with an increase in capacity being caused by side reactions (SEI formation), rather than being due solely to sodium occupancy of defect sites. ^{23}Na solid-state NMR[31] demonstrates that sodium initially inserted at higher voltages is ionic in nature, becoming progressively more metallic as sodiation proceeds, and is interpreted as initial attachment to pore walls and near interlayer defects, followed by intercalation and insertion into pores near defects occurring at lower voltages. Small angle X-ray Scattering (SAXS) studies[11, 25, 32] conclude that the sloping region of the voltage profile is due to sodium intercalation between graphene layers in the TNDs and attribute the plateau region below 100 mV to occupation of the pores between the TNDs. X-Ray Diffraction (XRD) investigations have proved inconclusive in the literature; the lack of long range order found in hard carbon results in broad, weak diffraction peaks, making it difficult to resolve accurately intensity changes and peak shifts, such as the well-defined shifts found for graphite intercalation compounds (GICs) upon intercalation as the graphitic layers move apart. Intercalation in the plateau region of the voltage profile has been inferred from a small increase in d-spacing between graphene layers over this region, [21, 33] however, in these cases d-spacing actually starts to increase over the sloping region. In other work, a decrease in the 002 peak intensity has been observed over the sloping region during sodiation, which then reversed on desodiation,[30,32] and since the 002 peak does not shift to higher d-spacing, this result has been interpreted as adsorption onto the surface of the hard carbon domain sheets rather than intercalation.[30] However, surface adsorption should not change the relative intensity of the 002 graphite

4

peak and the reduction in 002 peak intensity could indicate intercalation if the resulting intercalated domains are suitably disordered.

Raman scattering has emerged as a powerful technique to investigate the nanoscale structure, intercalation, disorder and carrier concentration of carbon-based materials.[34-48] The positions, widths, relative intensities and peak shapes of the characteristic G-peak and D-peak reveal the degree of interlayer stacking and disordering of the carbon, as well as indicating electron transfer from intercalated species into the graphene-derived conduction bands.[34] While numerous groups have published *in situ* and operando Raman spectroscopy studies for the insertion of lithium into graphite and other carbons,[38-48] for the sodiation of hard carbon only a limited number of Raman studies have been reported to date.[11, 18, 20, 22, 49-51] Moreover, ex situ studies have been limited to only a few data points during sodiation[11] or measurements carried out in ambient air,[22, 49] which we show adversely affects the results since the sodium de-intercalates. A recent study[50] combined operando Raman spectroscopy and Density Functional Theory (DFT) calculations to investigate the sodiation mechanism of coconut-shell derived hard carbon, supporting the picture that intercalation into the TNDs occurs during the sloping part of the voltage profile. However, the decrease in G-peak energy upon sodiation of that material was not fully reversible on desodiation, suggesting that complete deintercalation did not occur. Furthermore the D-peak analysis was inhibited since the resonant process associated with the appearance of this peak was blocked upon intermediate doping due to the laser energy. There was also no correlation reported between the Raman spectra and the formation of the SEI. Elsewhere, *in situ* Raman spectroscopy has been used to investigate the sodiation mechanism in nitrogen-doped hard carbon,[51] however, these materials showed no lower voltage plateau, but only a sloping voltage profile over the full range. A decrease in G-peak energy was observed from 1-0.02 V, but this decrease was only attributed to sodium intercalation in the lower voltage region, below 0.3 V.

Herein, a detailed operando Raman study of the sodiation and desodiation of a commercial hard carbon is presented, measuring at frequent intervals, during the initial formation cycle and again after several cycles. Peak fitting of the spectra permits the deconvolution of the G-peak, D-peak and background and the extracted trends clearly demonstrate that the sloping region of the voltage profile is due to the intercalation of sodium ions into the TNDs. Through judicious choice of laser energy, a gradual change of the D-peak is monitored throughout the sodiation process and shown to be fully reversible, with an unchanging D/G peak intensity ratio. The non-changing graphitic phonon energies over the low voltage plateau suggests no further net intercalation occurs in this region. Further, a region of the profile is found where the Solid Electrolyte Interphase (SEI) forms, with a subsequent increase in background slope in the spectra suggesting the possibility of tracking and quantifying the changes in the spectra due to SEI formation.

2. Results

Optical cells for operando Raman spectroscopy were assembled, as shown in **Figure 1** (a), using a hard carbon anode working electrode in contact with the bottom plunger, and sodium metal counter electrode. The sodium metal counter electrode and the separator both had central holes, to allow the laser beam to pass through to the surface of the working electrode below; further details of cell assembly are given in the Experimental section. Cells were tested at C/5 or C/3, based on a specific capacity of 300 mA h g^{-1} for hard carbon on the initial cycle, where C/x denotes the current required to discharge the cell in x hours.

Raman spectra were recorded during sodiation and desodiation. The laser power and sample exposure were optimised in order to achieve a sufficient signal-to-noise ratio whilst ensuring the sample was not

6

damaged by the beam, which can result in a large resonant signal.[52] Since spectra were recorded without pausing the current, the time taken to acquire each spectrum was kept as short as possible (while achieving a signal with adequate signal-to-noise for data fitting), which was typically in the range 0.03-0.6% of capacity. Figure 1 (b)-(e) show optical images of the hard carbon surface before filling the optical cell with electrolyte, and before and after the initial sodiation and subsequent desodiation, illustrating the change in the carbon surface after electrolyte filling and SEI formation. Owing to the difficulty in focussing on the carbon surface, and in order to ensure that spectra were representative of the entire surface, the laser was directed onto different spots on the electrode during discharge (sodiation) and charge (desodiation), and refocussed manually for each spot. This approach allowed numerous spectra to be recorded over several hours without burning the sample. The background slope and the G- and D-peak parameters were extracted from the spectra by peak fitting with custom software, as described in the Experimental section.
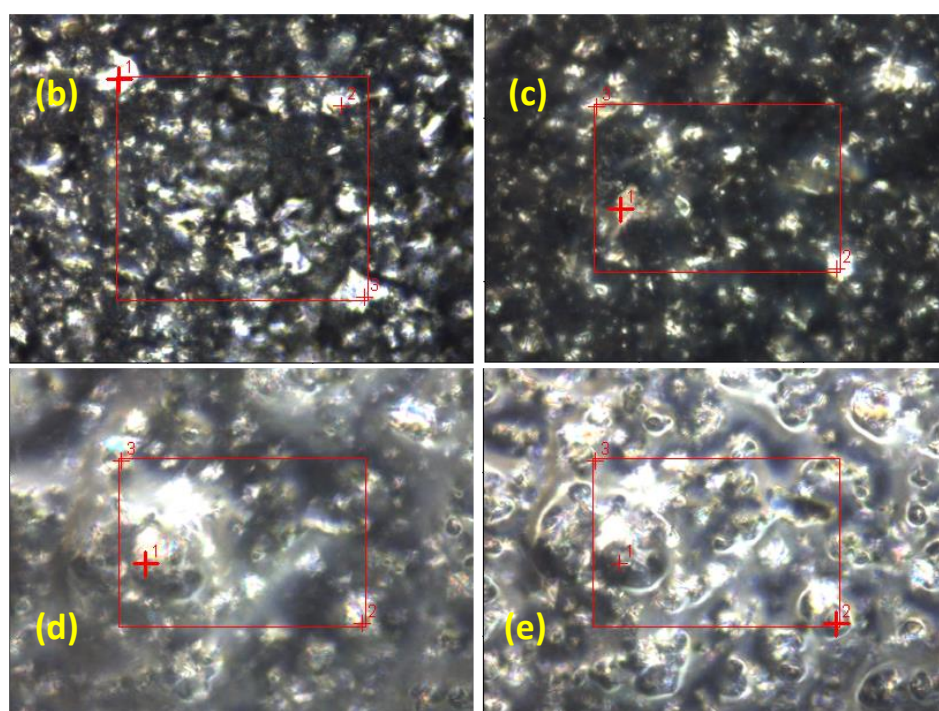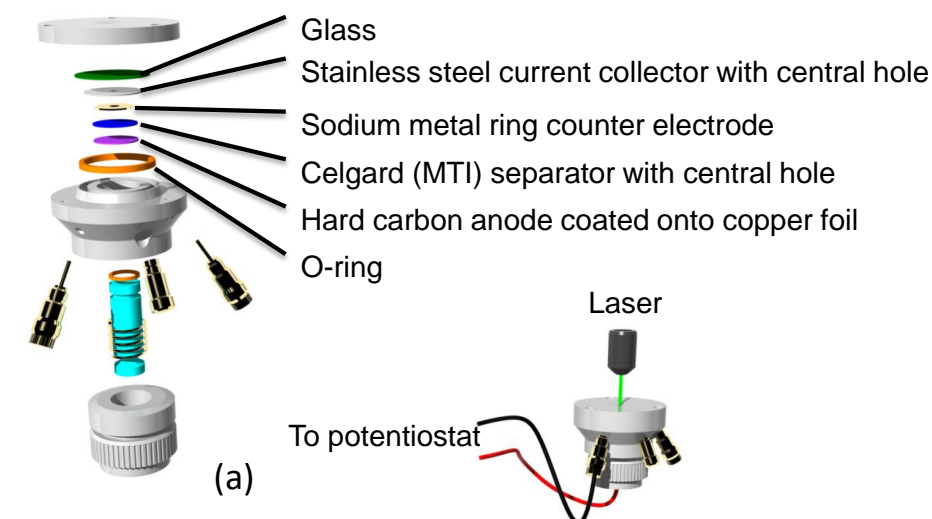
Figure 1 (a) Optical cell configuration (El-Cell® ECC-Opto-Std) used in this study; (b)-(e) *in situ* optical images, taken with 50x magnitude long working distance lens, of hard carbon electrode surface as observed when focussing through the glass into the optical cell; (b) fresh, dry cell (before filling with electrolyte); (c) after electrolyte addition (pre-sodiation); (d) end of sodiation at C/3 to 5 mV (there was no constant voltage hold); (e) end of subsequent desodiation, at C/3 to 3 V; C/3 based on 300 mA h g^{-1} for hard carbon.

Examples of selected spectra recorded during sodiation are shown in **Figure 2**. The G-peak at ~1590 cm^{-1} corresponds to the first order Raman scattering from an in-plane E_{2g} symmetry phonon in-plane of the crystalline graphene sheets, whereas the D-peak (~1350 cm^{-1}) corresponds to the in-plane optical phonon close to the K-point in the graphene Brillouin zone and is activated by disorder scattering.[35-37] Both peaks are found to broaden and shift to a lower wavenumber during sodiation with the reverse trend on desodiation. Additionally, during the initial sodiation, there is a non-reversible increase in the slope of the background. The G- and D-peak parameters and the background slope, extracted from the fits to the spectra, are superimposed onto the voltage profile in **Figure 3** and **Figure 4**, allowing changes in Raman spectra to be directly compared to features in the voltage profile during the first (formation) cycle and after cycling (cycle-9).
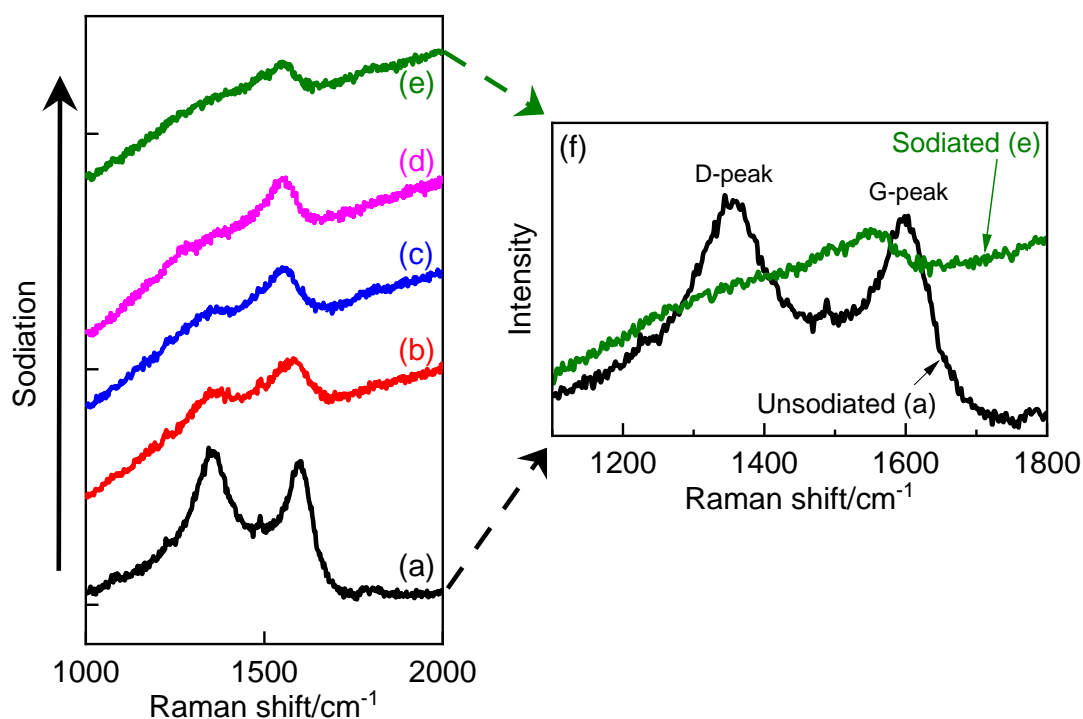

Figure 2 Example spectra recorded during sodiation of cycle-1, illustrating the changes in the G-peak and D-peak; note that the background slope increases after SEI formation on the initial sodiation; test

9

conditions given in Figure S3; (a) pre-sodiation, (b) 65 mA h g⁻¹, (c) 115 mA h g⁻¹, (d) 172 mA h g⁻¹, (e) 263 mA h g⁻¹, (f) expanded spectra from (a) and (e).
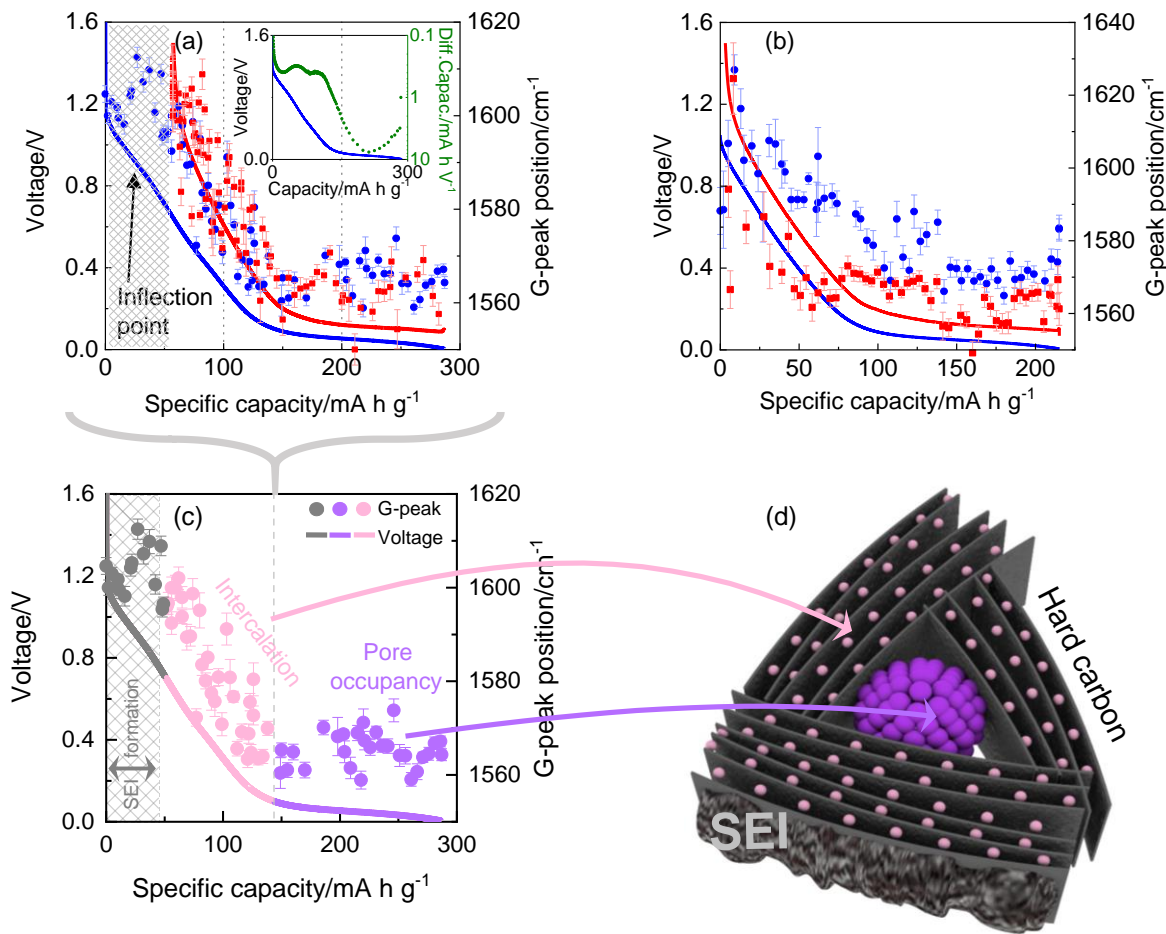

Figure 3 Voltage profiles and G-peak position obtained from peak fitting spectra from operando Raman experiment for discharge (sodiation) and subsequent charge (desodiation) of sodium-hard carbon cell on (a) cycle-1 and (b) cycle-9; sodiation shown in blue, desodiation shown in red; First Cycle Loss associated with SEI formation shown in grey shading in (a) and the inflection point in the voltage profile associated with SEI formation is indicated by an arrow in (a); solid line = voltage profile, discrete points = G-peak position (blue dots =sodiation, red squares = desodiation); inset graph in (a) shows differential

capacity (green) and voltage (blue) versus specific capacity; sodiation was carried out by discharging at constant current of C/5 to 5 mV (there was no constant voltage hold) and desodiation was at a constant current charge at C/5 to 1.5 V; C/5 for cycle-1 was based on 300 mA h g^{-1} for hard carbon, C/5 for cycle-9 was based on cycle-1 charge capacity; (c) voltage profile (solid line) and G-peak position (discrete points) for discharge of cycle-1, taken from (a), indicating regions of SEI formation (grey shading), intercalation (light pink) and pore occupancy (violet); (d) stylised visualisation (not to scale) illustrating sodiation mechanism in hard carbon: intercalation (light pink) between graphene layers occurs over the sloping region and pore occupancy (violet) occurs over the low voltage plateau of the discharge curve shown in (c). The approximate dimensions of the model in (d) are consistent with those commonly reported for hard carbon comprising curved TNDs with crystallite size dimensions ~1-2 nm (out of plane) and ~2-4 nm (in plane) encasing micropores with dimensions of < 2 nm in diameter in which sodium clusters form.[29, 31, 33]
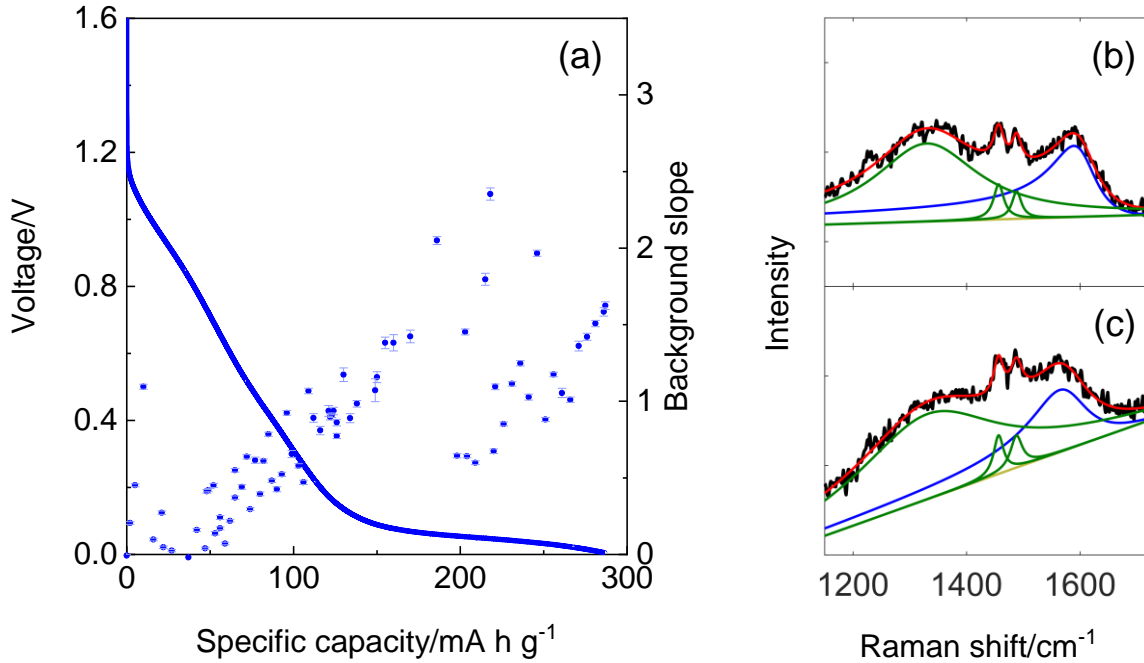
Figure 4 (a) Background slope plotted with the voltage profile against specific capacity during discharge (sodiation) on cycle-1 of the cell in Figure 3; solid line = voltage profile, discrete points = background slope; (b)-(c) selected spectra recorded at different capacities during sodiation: (b) 22 mA h g^{-1}, (c) 106 mA h g^{-1}; the small peaks at 1457 cm^{-1} and 1487 cm^{-1} arise from the electrolyte and are occasionally observable depending on cell/electrode alignment, data (black), total fit (red), Lorentzian fit (green), Breit-Wigner-Fano fit (blue), background (dark yellow).

2.1. Changes in G-peak and D-peak upon sodiation and desodiation

Figure 3 (a) shows the extracted G-peak position plotted alongside the voltage profile for the initial sodiation at C/5. The most notable feature of the data in Figure 3 is the striking correlation between the change in the G-peak energy and the voltage profile. However, during the initial sodiation only (cycle-1, blue data points Figure 3 (a), and grey data points in Figure 3 (c)), the G-peak energy remains relatively constant at ~1600-1610 cm^{-1} over the first ~50 mA h g^{-1}. In this region, also for the first cycle only, an

inflection point at ~0.9 V is found in the voltage profile (indicated by the arrow in Figure 3 (a)) and more clearly visible as a peak in differential capacity (Figure 3 (a) inset). This region closely corresponds with the first cycle loss (indicated by the grey rectangle in Figure 3 (a) and (c)), and has been attributed to SEI formation reactions.[53-54] The sodium SEI forms at around 0.8 V vs Na/Na$^+$ [53]resulting from the decomposition of the organic carbonates in the electrolyte on the pristine carbon surface, and by reaction of the NaPF$_6$ salt with sodium passing through the interface. Once a stable SEI has formed, further electrolyte decomposition is prevented. Indeed, the inflection point is not apparent on cycle-9 in Figure 3 (b), consistent with no further decomposition. As explained in detail below, the unchanging G-peak energy over the first ~50 mA h g^{-1} of the initial sodiation precludes the possibility that the first cycle loss could be due to intercalated sodium being trapped in the carbon, making it unavailable for subsequent cycles because, if this was case, the energy of the G-peak would change in this region. It is also possible that some part of this irreversible capacity is due to sodium irreversibly reacting with edge states and defects on the carbon.

Following SEI formation (and also for subsequent cycles), the G-peak steadily and substantially decreases in energy, at approximately 0.5 cm^{-1} per mA h g^{-1}, until roughly 1560 cm^{-1}, directly coincident with the sloping region of the voltage profile, from ~0.7 V to ~0.1 V (~50 mA h g^{-1} to ~135 mA h g^{-1}), before finally showing no change over the final flat part of the voltage profile (the low voltage plateau). Notably this change is reversible (upon desodiation) and persists upon subsequent cycles (Figure 3 (b)). Alongside changes in the G-peak energy, changes in width are similarly reversible (Figure S1), with an initial broadening of the peak followed by a decrease in width.

The G-peak energy and width are well-known to be highly sensitive to doping. A similar drastic decrease in energy of the G-peak phonon concomitant with an increase in width have been measured for alkali metal graphite intercalation compounds (GICs) of known stoichiometry.[15, 34, 52, 55] The downshift

results from the charge transfer from the alkali metal atoms to π^* anti-bonding orbitals of the carbon structure, which results in the lengthening of the C-C bonds (as measured by X-ray diffraction) thus reducing the G-peak energy, alongside a non-adiabatic renormalization of the phonon energy due to strong electron-phonon interactions,[52, 55-57] which also modifies the phonon lifetime and therefore the width of the peak.[57] In this way, the Raman spectra of graphitic compounds are unusually sensitive to electron doping due to a combination of high frequency phonon modes and the unique band structure of graphene.[55, 57] A similar effect is found for mono to few layer graphene upon heavy electron doping (though here, initial doping increases the G-peak energy due to a removal of the Gamma point Kohn anomaly in undoped graphene), achieved by alkali metal adsorption.[55, 58] However, in stark contrast to GICs, for which the downshift in energy is distinct for different compounds with fixed metal:carbon ratio, the graphene G-peak energy shift decreases monotonically with increasing alkali metal coverage. The gradual and tunable effect on the average phonon energy indicates that the charge transfer is homogenously delocalized across the graphene, as expected for metallic, electron-doped graphene sheets.[56, 59] However, flakes thicker than a few layers revert to distinct spectra from stoichiometric compounds found in GICs, similar to the Li-intercalation in graphite for batteries. The tunability that is observed in the hard carbon-sodium system is, therefore, similar to few layer graphene and the gradual (reversible) decrease in the G-peak position can be understood as to be due to electron doping resulting from intercalation as the sodium is incrementally added and spreads uniformly through the layers as shown in light pink in Figure 3(d). A similar trend has been observed for the lithiation of activated,[39] disordered[42] and pyrolytic[45] carbons. Intercalation of alkali metals into graphitic species is known to be driven by a complete charge transfer of the valance electron from the metal species into the graphene-derived electron bands (sometimes including the formation and occupation of a new interlayer band).[56, 60] As such the intercalated alkali metal is ionic as measured by recent ^{23}Na NMR measurements of the sodium/hard carbon system in the sloping part of the voltage profile.[31] It has been suggested that in this

region sodium is adsorbed onto the TNDs' surfaces, rather than being also intercalated.[30] While it is true that surface adsorbed sodium would cause a similar G-peak shift to lower energy, if this was the sole doping mechanism, the G-peak would split into two peaks resulting from the presence of adjacent intercalated and non-intercalated graphene layers, similar to that found for stage 3 or higher GICs, given that the typical TNDs are comprised of < 5 layers.[29,38, 61-64,65] No splitting of the G-peak is observed in this work, therefore, intercalation must be occurring over the sloping region. Here we note that this G-peak shift is insensitive to whether the Na preferentially intercalates at defect sites where calculations predict (reversible) charge transfer is stronger[50,66], if these sites are homogeneously distributed. Following the initial decrease, the G-peak energy remains constant over the long, low voltage plateau, indicating that no further net intercalation occurs in this region, again consistent with ^{23}Na NMR results, which show the increased metallicity of the sodium species i.e. as metallic sodium forms in the pores. This is illustrated in violet in Figure 3(d).

The G-peak width, the D-peak position and width, as well as the ratio of intensities (I_D/I_G), are given in Figure S1 in the Supplementary Information. Similar to the G-peak, the D-peak energy and width remain constant over the initial period of SEI formation. After this, there is a gradual decrease of the D-peak energy and change of width upon sodiation. Notably, as with the G-peak, this trend is reversible upon desodiation, indicating that the changes again result from a change in the phonon energies and lifetimes from the electron doping of the graphene sheets[52, 55, 60], rather than any increase in disorder developing in the carbon lattice itself, for example by bond-breaking, which would not be reversible. It should also be noted that the I_D/I_G ratio, which indicates disorder, remains relatively constant throughout the sodiation/desodiation cycle.

These distinctive trends in G- and D-peaks upon sodiation/desodiation were found in numerous samples. For example Figure S2 shows data recorded for the initial sodiation of a cell atC/3, Figure S3 show results for the initial sodiation and subsequent desodiation of another cell at C/5 and Figure S4 shows results for the initial sodiation and subsequent desodiation of a cell at C/3.

2.2. Changes in spectra upon cycling

The experiment was repeated after cycling at C/5 and the data for G-peak position and voltage profile for cycle-9 is shown in Figure 3 (b). Again, during sodiation the G-peak decreases linearly, at approximately 0.5 cm^{-1} per mA h g^{-1}, to a lower wavenumber (~1570 cm^{-1}) over the sloping voltage profile, until ~80 mV (~110 mA h g^{-1}). The G-peak then returns to its original energy on the subsequent charge (desodiation) of cycle-9, as reported for cycle-1. However, for cycle-9 the "plateau" in G-peak position at the start of sodiation is absent, consistent with the assignment of this plateau to SEI formation on the first cycle. The trends in G-peak width, D-peak position and width and the ratio of intensities (I_D/I_G) for cycle-9 are also consistent with cycle-1 and are given in **Figure S5** of the Supplementary Information. As on cycle-1, the D-peak changes are reversible, suggesting no increase in disorder in the carbon structure. In Fig 3b, a small hysteresis of the position of G-peak energy in cycle-9 can be seen, with a shallower G-peak dependency on sodiation compared to desodiation which is not mirrored in the voltage profile or evident in cycle-1. This observation potentially suggests that after multiple cycling, during sodiation there is a small degree of pore filling occurring concomitant with the intercalation during the sloping part of the voltage profile. However, it should be noted that after multiple cycles the Raman spectra are increasingly challenging to record due to difficulty focusing giving noisier spectra (evident from the larger error bars on the fit-extracted G-peak energies) and thus further work is required to investigate this effect.

Together with the plateau in the G-peak position, another change on cycle-1, which is absent on subsequent cycles, is found in the nature of the spectral background. During sodiation on cycle-1 a clear increase in the background slope of spectra is observed. This effect is shown in **Figure 4**, where the background slopes of the spectra are superimposed onto the voltage profile for sodiation in Figure 4 (a) and selected spectra at different stages of sodiation are shown in Figure 4 (b)-(c). The background slope superimposed onto the voltage profile for desodiation is given in **Figure S6** of the Supplementary Information. The change in background is not reversed on the first desodiation, and remains on multiple cycling (cycle-9, **Figure S7**). Examination of the cycle-1 increase reveals that the background is relatively flat over the initial ~50 mA h g^{-1}, i.e., before SEI formation. The significant increase in background slope can be understood as a result of increased fluorescence from the SEI. Also, the electrolyte peaks at approximately 1457 cm^{-1} and 1487 cm^{-1} in Figure 4 (b)-(c) fade and are no longer apparent in subsequent spectra (Figure S7), possibly due to electrolyte decomposition during SEI formation. A similar increase in background slope, and decrease in electrolyte peak signal, has been noted previously for lithium systems.[43]

2.3. Effect of washing electrodes in electrolyte solvent, propan-2-ol and after exposure to air

Figure 5 (a)-(d) show Raman spectra recorded at the end of sodiation and then following various washes. For these experiments, the hard carbon electrode was removed in a glovebox (without air exposure), washed first in diethyl carbonate (DEC), dried and then reloaded in the optical cell, without air exposure, for measurement. The process was then repeated using propan-2-ol (IPA). Finally, the optical cell was opened to the air and spectra were recorded in the open atmosphere. The G- and D-peak position and width, together with the ratio of intensities (I_D/I_G) and background slope, are plotted in Figure 5 (e)-(j). Washing the sample in diethyl carbonate (DEC), which is a component of the electrolyte (Figure 5 (b)), removes the peak at approximately 900 cm^{-1}, which is attributed to ethylene carbonate

(EC), also a component of the electrolyte, coordinated with the metal ion.[43] Washing the samples in IPA (which reacts with sodium) causes significant changes to the Raman spectra, due to SEI removal and sodium de-intercalation. It can be seen that the background of the spectra flattens, which indicates that the SEI has been removed or damaged by the mechanical washing process, thus reducing fluorescence. The SEI in sodium systems is known to be more soluble and less stable than in Li-ion systems.[10] In addition to a reduction in the background slope the G- and D-peaks shift back to their original energies (i.e. prior to sodiation). These changes are then augmented when the electrode is exposed to air.

The shift in G- and D-peaks back toward their initial positions, indicates a full de-intercalation of ionic sodium from the TNDs, with a sharpening of the D-peak and an increase in its intensity as indicated by an increase in I_D/I_G. The reversibility in the D-peak character after washing in IPA and exposure to air confirms that the changes that manifest upon sodiation are not caused by a permanent increase in disorder in the hard carbon lattice. The substantial effect on the measured spectra of air exposure and washing the samples has important implications for *ex situ* Raman studies, where electrodes may be washed prior to study, and highlights that operando Raman studies are required for investigating sodiation mechanisms, for example, *ex situ* studies,[49] where sodium intercalation is discounted due to the absence of the G-peak shift, may be misleading as the results are likely to be adversely affected by washing and air exposure.
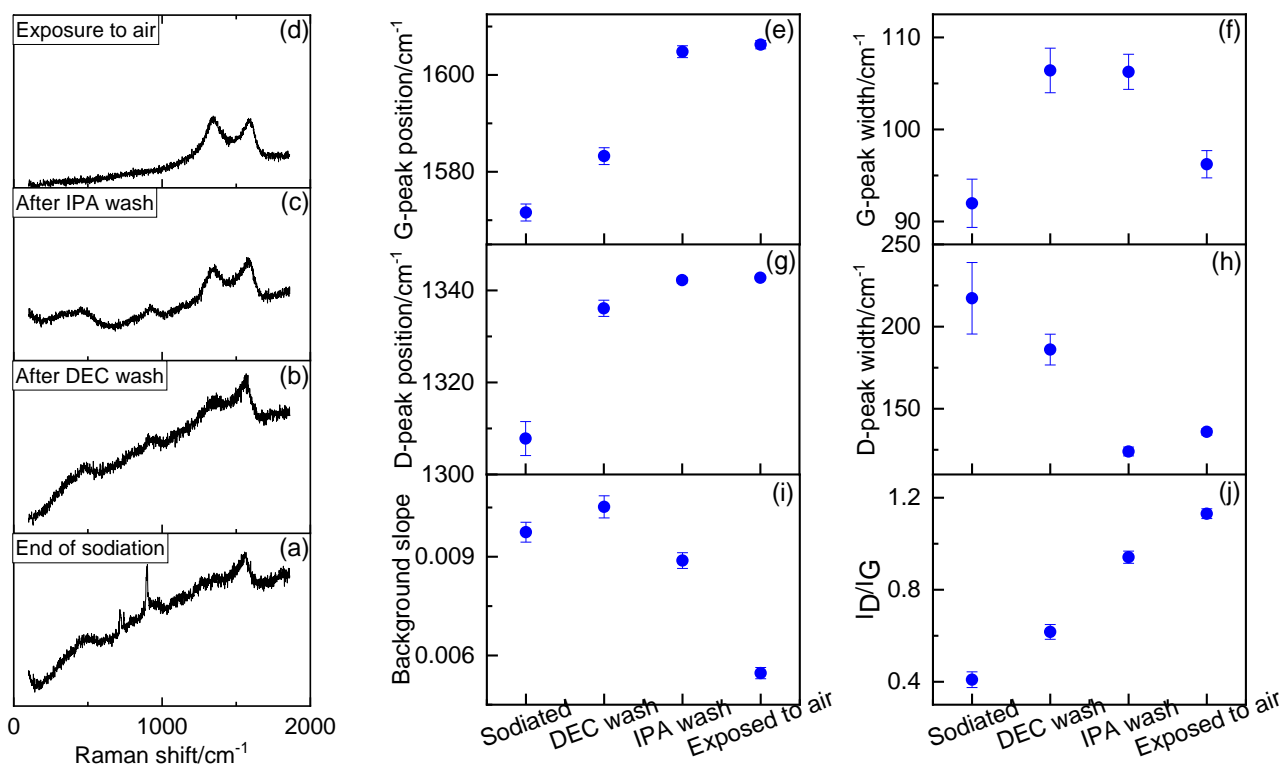
Figure 5 (a)-(d) Raman spectra measured for samples as follows: (a) end of sodiation, in sealed cell; (b) washed in diethyl carbonate (DEC), dried, then transferred to sealed cell, all within the glove box; (c) washed in propan-2-ol (IPA), dried, then transferred to sealed cell, all within the glove box; (d) sample removed from sealed cell and Raman spectra measured in open atmosphere; (e)-(j) parameters extracted from spectra, after various washes as follows: (e) G-peak position, (f) G-peak width, (g) D-peak position, (h) D-peak width, (i) background slope and (j) ratio of intensities I_D/I_G.

3. Discussion and Conclusions

Operando Raman spectroscopy has proved a critical tool in elucidating several key aspects of the sodiation mechanism in hard carbon, unachievable for other, less direct methods or those that focus solely on the sodium. Most importantly, the gradual and reversible changes in the G- and D- graphitic Raman peaks confirm that sodium uptake, associated with the initial, sloping part of the voltage profile, arises from intercalation into the TNDs. Moreover, these results rule out that it is only the surface of these

domains that are occupied, and suggest that the capacity derives from full intercalation and associated charge transfer to the graphene-derived electronic bands, with association/chemical bonding onto defects therefore only playing a minor role in this region. The G-peak position remains essentially of constant energy over the long, low voltage plateau, suggesting no further significant doping of the graphitic bands that would result from more intercalation, and thus the capacity in this region is due to sodium cluster formation within the pores. This region of the voltage profile is hindered by slow diffusion[17, 21] and is more susceptible to capacity losses that would arise from increased resistance, suggesting that improvements in rate performance and capacity retention with cycling should focus on careful pore design when considering novel hard carbon materials. To control pore structure it has been found that with increasing carbonization temperature, there is a decrease in d-spacing, surface area and micropore (<2 nm) volume, while the mesopore (>2 nm) volume increases.[21-23, 30, 33, 49] Heating apparently reduces the number of micropores as well as removing heteroatoms present.[23, 30] The negative correlation between microporosity and low voltage plateau capacity has previously been used to refute the hypothesis that the plateau is due to pore occupancy, [23, 33] however, the insight from the operando Raman studies reported here, supports conclusions that it is the mesopores that accommodate sodium insertion at low voltages.[30] The diffusion coefficients for the sodiation/desodiation of hard carbon have a distinct profile. Although values vary in magnitude for different systems,[17, 21, 23-24] there is general agreement that the diffusion coefficients are higher over the sloping region of the voltage profile and lower over the low voltage plateau. The unique structure of the TND domains in hard carbon, when compared to ordered graphite, not only enables the intercalation of sodium, but gives rise to an intercalation process that is more similar to that found for few layer graphene than graphite. Importantly, this means that intercalant ions can be incrementally added, implying that distinct sites resulting from stoichiometrically-fixed intercalated graphite are less well defined in hard carbon, consistent with relatively fast intercalation.

The intrinsic disorder of the intercalated species also explains the lack of distinct/uniform layer separation or identification of alkali metal superlattice formation in XRD.

The reversibility of the D-peak arises from intercalation/de-intercalation into the carbon structure, rather than reflecting the development of irreversible damage or increase in disorder to the structure. Therefore, monitoring the D-peak reversibility over long-term cycle life studies could be a valuable tool for identifying and investigating any breakdown in the carbon structure, expected over long term cycling, and the degree to which this may contribute to capacity loss. Finally, operando Raman spectroscopy also provides information on the SEI formation, with little change of Raman spectra upon first sodiation alongside the development of a sloped background as the SEI forms. Washing the electrode in propan-2-ol and exposing the samples to air cause the background to flatten again, demonstrating the SEI can be removed by the washing process. The changing background can, therefore, potentially be used to evaluate SEI formation and stability, though further work is required in this area to understand this observation. Finally, this work cautions the use of *ex situ* studies to investigate the sodiation mechanism, because air-exposure or washing is shown to remove or change features that arise during this process.

4. Experimental Section

Hard carbon structure. A commercial, plant based hard carbon was used with a disordered structure. Previous work on the same material,[65] deduced a structure of inaccessible micropores surrounded by graphene sheets, with interlayer spacing d_{002}~0.38 nm.

Preparation of electrodes. Hard carbon electrodes were prepared containing ~88 wt% hard carbon (Commercial) + ~7 wt% PVDF binder (Solef 6020) + ~5 wt% carbon black electronic additive (Timcal C45). The hard carbon and C45 powders were added to a solution of PVDF in NMP, and mixed using a

T-25 Ultra Turrax high-shear mixer; the speed was increased slowly whilst adding the powders, ensuring the mix temperature did not become warm to the touch. The slurry was coated onto copper foil at a fixed blade gap of either 100 or 150 µm. The coating was pre-dried under an halogen heating lamp, then dried under vacuum at $80^{\circ}C$ for three hours. Electrode discs were cut from this coating and dried under vacuum for a further six hours at $80^{\circ}C$, before being allowed to cool to room temperature under vacuum overnight. Electrodes were not calendered.

Cell fabrication. Prior to use, all components were dried at $50\text{-}60^{\circ}C$ in a Buchi drying tube, before transferring to an argon-filled glove box (M Braun) for cell construction.

An El-Cell® ECC-Opto-Std optical test cell was used for operando Raman studies. The cell configuration is shown in Figure 1. The hard carbon electrode under study had a diameter of 10 mm and was placed in contact with the lower current collector plunger, followed by one layer of Celgard (MTI) separator, with a central hole and a ring of sodium metal (counter electrode) (Sigma Aldrich) pressed onto a stainless steel current collector disc, also with a central hole. A standard glass window and steel top cap completed the assembly. The cell was filled with 1 M $NaPF_6$ in EC:DEC (1:1) electrolyte (Koshida) using a syringe to apply a vacuum prior to releasing an excess of electrolyte into the cell.

Electrochemical testing. Cells were tested using either a Gamry Instruments Interface 1000 potentiostat or a Maccor Series 4000 desktop unit, at C/3 or C/5, based on a rated capacity of 300 mA h g^{-1} for hard carbon. Details of the sodiation and desodiation test protocols are given in the figure captions for each test. Note that in sodium metal "half-cells", such as those reported in this work, sodiation occurs during discharge (negative current), but occurs during charge in a full sodium-ion cell.

In order to reduce noise, differential capacity was calculated for a change in voltage of at least 5 mV. Differential capacity was plotted on a $\log_{10}$ scale, in order to show the peak structure over a large range.

Raman spectroscopy. Operando Raman spectroscopy was carried out using a ThermoScientific DXR Raman Microscope fitted with a 532 nm laser. Spectra in Figure 3, Figure 4, Figure S1, Figure S5, Figure S6 and Figure S7 were recorded using a 50x magnification long working distance (LWD) lens and laser power kept below 6 mW. On the initial sodiation each spectrum covered ~0.06% of discharge (sodiation) capacity (0.5 second sample times and 20 samples averaged for each spectrum). For the subsequent desodiation on cycle-1 each spectrum covered ~0.04 % of charge (desodiation) capacity (0.3 second sample times and 20 samples averaged for each spectrum). For both sodiation and desodiation on cycle-9, each spectrum covered ~0.04 % of discharge (sodiation) or charge (desodiation) capacity (0.3 second sample times and 20 samples averaged for each spectrum).

Spectra in Figure S2 were recorded using a 50x magnification long working distance (LWD) lens and laser power kept below 4 mW; each spectrum covered ~0.1 % of discharge (sodiation) capacity (1 second sample times and 10 samples averaged for each spectrum).

Spectra in Figure 2, Figure S3 and Figure S4 were recorded using a 10x magnification long working distance (LWD) lens and laser power kept below 6 mW. For Figure 2 and Figure S3 each spectrum covered ~0.3% of discharge (sodiation) capacity and ~0.4% of charge (desodiation) capacity (5 second sample times and 10 samples averaged for each spectrum). For Figure S4 each spectrum covered ~0.5% of discharge (sodiation) capacity and ~0.6% of charge (desodiation) capacity (5 second sample times and 10 samples averaged for each spectrum).

23

Spectra in Figure 5 were recorded using a high resolution grating and 532 nm laser, 10x magnification short working distance (SWD) lens and laser power kept below 6 mW. Each spectrum was averaged over ten 5 second samples.

Peak deconvolution was carried out using custom developed software. The D-peak was fitted at ~1350 cm^{-1} using a Lorentzian function and the G-peak was fitted at ~1600 cm^{-1} using a Breit-Wigner-Fano (BWF) function, which approximated a Lorentzian fit, but included an asymmetry term, which was found to be most appropriate for the G-peak.[55]   The background was taken as a straight line in the window of the fit.

ASSOCIATED CONTENT

Supporting Information

The Supporting Information is available free of charge:

PDF document containing extra Raman spectroscopy data for the experiments reported in the main text, as well as data from additional experiments, demonstrating consistency of results.

AUTHOR INFORMATION

Corresponding Authors

* c.howard@ucl.ac.uk, * d.brett@ucl.ac.uk.

Notes

The authors declare no conflict of interest.

ACKNOWLEDGEMENT

REFERENCES

(1) Pan, H.; Hu, Y. S.; Chen, L. Room-temperature stationary sodium-ion batteries for large-scale electric energy storage. *Energy & Environmental Science* **2013,** *6* (8), 2338-2360

(2) Ellis, B. L.; Nazar, L. F. Sodium and sodium-ion energy storage batteries. *Current Opinion in Solid State and Materials Science* **2012,** *16* (4), 168-177

(3) Roberts, S.; Kendrick, E. The re-emergence of sodium ion batteries: testing, processing, and manufacturability. *Nanotechnol Sci Appl* **2018,** *11*, 23-33

(4) Smith, K.; Treacher, J.; Ledwoch, D.; Adamson, P.; Kendrick, E. Novel High Energy Density Sodium Layered Oxide Cathode Materials: From Material to Cells. *ECS Transactions* **2017,** *75* (22), 13-24

(5) Kubota, K.; Komaba, S. Review—Practical Issues and Future Perspective for Na-Ion Batteries. *Journal of The Electrochemical Society* **2015,** *162* (14), A2538-A2550

(6) Slater, M. D.; Kim, D.; Lee, E.; Johnson, C. S. Sodium-Ion Batteries. *Advanced Functional Materials* **2013,** *23* (8), 947-958

(7) FaradionLtd. In *Progress in the Commercialization of Faradion's Na-ion Battery Technology*, 4th International Meeting on Sodium Batteries, Shinjuku, Tokyo, Japan, 2017.

(8) Robinson, J. B.; Finegan, D. P.; Heenan, T. M. M.; Smith, K.; Kendrick, E.; Brett, D. J. L.; Shearing, P. R. Microstructural Analysis of the Effects of Thermal Runaway on Li-Ion and Na-Ion Battery Electrodes. *Journal of Electrochemical Energy Conversion and Storage* **2018,** *15* (1), 011010

(9) Robinson, J. B.; Heenan, T. M. M.; Jervis, J. R.; Tan, C.; Kendrick, E.; Brett, D. J. L.; Shearing, P. R. Multiscale tomographic analysis of the thermal failure of Na-Ion batteries. *Journal of Power Sources* **2018,** *400*, 360-368

(10) Mogensen, R.; Brandell, D.; Younesi, R. Solubility of the Solid Electrolyte Interphase (SEI) in Sodium Ion Batteries. *ACS Energy Letters* **2016,** *1* (6), 1173-1178

(11) Komaba, S.; Murata, W.; Ishikawa, T.; Yabuuchi, N.; Ozeki, T.; Nakayama, T.; Ogata, A.; Gotoh, K.; Fujiwara, K. Electrochemical Na Insertion and Solid Electrolyte Interphase for Hard-Carbon Electrodes and Application to Na-Ion Batteries. *Advanced Functional Materials* **2011,** *21* (20), 3859-3867

(12) Oltean, V. A.; Philippe, B.; Renault, S.; Duarte, R. F.; Rensmo, H.; Brandell, D. Investigating the Interfacial Chemistry of Organic Electrodes in Li- and Na-Ion Batteries. *Chemistry of Materials* **2016,** *28* (23), 8742-8751

(13) Peled, E. The Electrochemical Behavior of Alkali and Alkaline Earth Metals in Nonaqueous Battery Systems - The Solid Electrolyte Interphase Model. *J electrochem soc* **1979,** *126* (12), 2047-2051

(14) Eshetu, G. G.; Grugeon, S.; Kim, H.; Jeong, S.; Wu, L.; Gachot, G.; Laruelle, S.; Armand, M.; Passerini, S. Comprehensive Insights into the Reactivity of Electrolytes Based on Sodium Ions. *ChemSusChem* **2016,** *9* (5), 462-471

(15) Dresselhaus, M. S.; Dresselhaus, G. Intercalation compounds of graphite. *Advances in Physics* **2002,** *51* (1), 1-186

(16) Stevens, D. A.; Dahn, J. R. High capacity anode materials for rechargeable sodium-ion batteries. *Journal of The Electrochemical Society* **2000,** *147* (4), 1271-1273

(17) Ledwoch, D.; Brett, D. J. L.; Shearing, P. R.; Kendrick, E. Investigation of the Sodiation and Desodiation of Hard Carbon by Electrochemical Testing and X-Ray Computed Tomography. *ECS Transactions* **2017,** *75* (52), 81-90

(18) Górka, J.; Vix-Guterl, C.; Ghimbeu, C. M. Recent Progress in Design of Biomass-Derived Hard Carbons for Sodium Ion Batteries. *C* **2016,** *2* (4), 24

(19) Irisarri, E.; Ponrouch, A.; Palacin, M. R. Review—Hard Carbon Negative Electrode Materials for Sodium-Ion Batteries. *Journal of The Electrochemical Society* **2015,** *162* (14), A2476-A2482

(20) Saurel, D.; Orayech, B.; Xiao, B.; Carriazo, D.; Li, X.; Rojo, T. From Charge Storage Mechanism to Performance: A Roadmap toward High Specific Energy Sodium-Ion Batteries through Carbon Anode Optimization. *Advanced Energy Materials* **2018**, 1703268

(21) Bommier, C.; Surta, T. W.; Dolgos, M.; Ji, X. New Mechanistic Insights on Na-Ion Storage in Nongraphitizable Carbon. *Nano Lett* **2015,** *15* (9), 5888-5892

(22) Lotfabad, E. M.; Ding, J.; Cui, K.; Kohandehghan, A.; Kalisvaart, W. P.; Hazelton, M.; Mitlin, D. High-density sodium and lithium ion battery anodes from banana peels. *ACS Nano* **2014,** *8* (7), 7115-7129

(23) Alvin, S.; Yoon, D.; Chandra, C.; Cahyadi, H. S.; Park, J.-H.; Chang, W.; Chung, K. Y.; Kim, J. Revealing sodium ion storage mechanism in hard carbon. *Carbon* **2019,** *145*, 67-81

(24) Wang, K.; Jin, Y.; Sun, S.; Shixiong; Huang, Y.; Peng, J.; Luo, J.; Zhang, Q.; Qiu, Y.; Fang, C.; Han, J. Low-Cost and High-Performance Hard Carbon Anode Materials for Sodium-Ion Batteries. *ACS Omega* **2017,** *2* (4), 1687-1695

(25) Stevens, D. A.; Dahn, J. R. An In Situ Small-Angle X-Ray Scattering Study of Sodium Insertion into a Nanoporous Carbon Anode Material within an Operating Electrochemical Cell. *Journal of The Electrochemical Society* **2000,** *147* (12), 4428-4431

(26) Luo, W.; Shen, F.; Bommier, C.; Zhu, H.; Ji, X.; Hu, L. Na-Ion Battery Anodes: Materials and Electrochemistry. *Acc Chem Res* **2016,** *49* (2), 231-240

(27) Wahid, M.; Puthusseri, D.; Gawli, Y.; Sharma, N.; Ogale, S. Hard Carbons for Sodium-Ion Battery Anodes: Synthetic Strategies, Material Properties, and Storage Mechanisms. *ChemSusChem* **2018,** *11* (3), 506-526

(28) Hwang, J. Y.; Myung, S. T.; Sun, Y. K. Sodium-ion batteries: present and future. *Chem Soc Rev* **2017,** *46* (12), 3529-3614

(29) Li, Z.; Bommier, C.; Chong, Z. S.; Jian, Z.; Surta, T. W.; Wang, X.; Xing, Z.; Neuefeind, J. C.; Stickle, W. F.; Dolgos, M.; Greaney, P. A.; Ji, X. Mechanism of Na-Ion Storage in Hard Carbon Anodes Revealed by Heteroatom Doping. *Advanced Energy Materials* **2017,** *7* (18), 1602894

(30) Zhang, B.; Ghimbeu, C. M.; Laberty, C.; Vix-Guterl, C.; Tarascon, J.-M. Correlation Between Microstructure and Na Storage Behavior in Hard Carbon. *Advanced Energy Materials* **2016,** *6* (1), 1501588

(31) Stratford, J. M.; Allan, P. K.; Pecher, O.; Chater, P. A.; Grey, C. P. Mechanistic insights into sodium storage in hard carbon anodes using local structure probes. *Chem commun* **2016,** *52* (84), 12430-12433

(32) Stevens, D. A.; Dahn, J. R. The Mechanisms of Lithium and Sodium Insertion in Carbon Materials. *Journal of The Electrochemical Society* **2001,** *148* (8), A803-A811

(33) Ding, J.; Wang, H.; Li, Z.; Kohandehghan, A.; Cui, K.; Xu, Z.; Zahiri, B.; Tan, X.; Lotfabad, E. M.; Olsen, B. C.; Mitlin, D. Carbon nanosheet frameworks derived from peat moss as high performance sodium ion battery anodes. *ACS Nano* **2013,** *7* (12), 11004-11015

(34) Chan, C. T.; Ho, K. M.; Kamitakahara, W. A. Zone-center phonon frequencies for graphite and graphite intercalation compounds: Charge-transfer and intercalate-coupling effects. *Physical Review B* **1987,** *36* (6), 3499-3502

(35) Ferrari, A. C. Raman spectroscopy of graphene and graphite: Disorder, electron–phonon coupling, doping and nonadiabatic effects. *Solid State Communications* **2007,** *143* (1-2), 47-57

(36) Ferrari, A. C.; Robertson, J. Resonant Raman spectroscopy of disordered, amorphous, and diamondlike carbon. *Physical Review B* **2001,** *64* (7), 075414

(37) Ferrari, A. C.; Robertson, J. Interpretation of Raman spectra of disordered and amorphous carbon. *Physical Review B* **2000,** *61* (20), 14095

(38) Sole, C.; Drewett, N. E.; Hardwick, L. J. In situ Raman study of lithium-ion intercalation into microcrystalline graphite. *Faraday Discuss* **2014,** *172*, 223-237

(39) Hardwick, L. J.; Ruch, P. W.; Hahn, M.; Scheifele, W.; Kötz, R.; Novák, P. In situ Raman spectroscopy of insertion electrodes for lithium-ion batteries and supercapacitors: First cycle effects. *Journal of Physics and Chemistry of Solids* **2008,** *69* (5-6), 1232-1237

(40) Hardwick, L. J.; Buqa, H.; Novak, P. Graphite surface disorder detection using in situ Raman microscopy. *Solid State Ionics* **2006,** *177* (26-32), 2801-2806

(41) Inaba, M.; Yoshida, H.; Ogumi, Z. In situ Raman Study of Electrochemical Lithium Insertion into Mesocarbon Microbeads Heat-Treated at Various Temperatures. *Journal of The Electrochemical Society* **1996,** *143* (8), 2572-2578

(42) Endo, M.; Kim, C.; Karaki, T.; Fujino, T.; Matthews, M. J.; Brown, S. D. M.; Dresslhaus, M. S. In situ Raman study of PPP-based disordered carbon as an anode in a Li ion battery. *Synthetic Metals* **1998,** *98*, 17-24

(43) Panitz, J.-C.; Novak, P.; Haas, O. Raman Microscopy Applied to Rechargeable Lithium-Ion Cells— Steps Towards in Situ Raman Imaging with Increased Optical Efficiency. *Applied Spectroscopy* **2001,** *55* (9), 1131-1137

(44) Hardwick, L. J.; Buqa, H.; Holzapfel, M.; Scheifele, W.; Krumeich, F.; Novák, P. Behaviour of highly crystalline graphitic materials in lithium-ion cells with propylene carbonate containing electrolytes: An in situ Raman and SEM study. *Electrochimica Acta* **2007,** *52* (15), 4884-4891

(45) Wang, Z.; Huang, X.; Xue, R.; Chen, L. A new possible mechanism of lithium insertion and extraction in low-temperature pyrolytic carbon electrode. *Carbon* **1999,** *37*, 685-692

(46) Pimenta, M. A.; Dresselhaus, G.; Dresselhaus, M. S.; Cancado, L. G.; Jorio, A.; Saito, R. Studying disorder in graphite-based systems by Raman spectroscopy. *Phys Chem Chem Phys* **2007,** *9* (11), 1276-1291

(47) Kostecki, R.; McLarnon, F. Microprobe study of the effect of Li intercalation on the structure of graphite. *Journal of Power Sources* **2003,** *119-121*, 550-554

(48) Sethuraman, V. A.; Hardwick, L. J.; Srinivasan, V.; Kostecki, R. Surface Structural Disordering in Graphite upon Lithium Intercalation/Deintercalation. *Journal of Power Sources* **2010,** *195* (11), 3655-3660

(49) Bai, P.; He, Y.; Zou, X.; Zhao, X.; Xiong, P.; Xu, Y. Elucidation of the Sodium-Storage Mechanism in Hard Carbons. *Advanced Energy Materials* **2018,** *8* (15), 1703217

(50) Anji Reddy, M.; Helen, M.; Groß, A.; Fichtner, M.; Euchner, H. Insight into Sodium Insertion and the Storage Mechanism in Hard Carbon. *ACS Energy Letters* **2018,** *3* (12), 2851-2857

(51) Zhong, X.; Li, Y.; Zhang, L.; Tang, J.; Li, X.; Liu, C.; Shao, M.; Lu, Z.; Pan, H.; Xu, B. High-Performance Sodium-Ion Batteries Based on Nitrogen-Doped Mesoporous Carbon Spheres with Ultrathin Nanosheets. *ACS Appl Mater Interfaces* **2019,** *11* (3), 2970-2977

(52) Dean, M. P. M.; Howard, C. A.; Saxena, S. S.; Ellerby, M. Nonadiabatic phonons within the doped graphene layers ofXC_6compounds. *Physical Review B* **2010,** *81* (4), 045405

(53) Yabuuchi, N.; Kubota, K.; Dahbi, M.; Komaba, S. Research development on sodium-ion batteries. *Chem Rev* **2014,** *114* (23), 11636-11682

(54) Dahbi, M.; Yabuuchi, N.; Kubota, K.; Tokiwa, K.; Komaba, S. Negative electrodes for Na-ion batteries. *Phys Chem Chem Phys* **2014,** *16* (29), 15007-15028

(55) Howard, C. A.; Dean, M. P. M.; Withers, F. Phonons in potassium-doped graphene: The effects of electron-phonon interactions, dimensionality, and adatom ordering. *Physical Review B* **2011,** *84* (24), 241404

(56) Yang, S.-L.; Sobota, J. A.; Howard, C. A.; Pickard, C. J.; Hashimoto, M.; Lu, D. H.; Mo, S.-K.; Kirchmann, P. S.; Shen, Z.-X. Superconducting graphene sheets in CaC6 enabled by phonon-mediated interband interactions. *Nat Commun* **2014,** *5*, 3493

(57) Kertesz, M. Changes of Lattice Geometries Upon Charge Transfer. *Molecular Crystals and Liquid Crystals* **1985,** *126* (1), 103-110

(58) Jung, N.; Kim, B.; Crowther, A. C.; Kim, N.; Nuckolls, C.; Brus, L. Optical Reflectivity and Raman Scattering in Few-Layer-Thick Graphene Highly Doped by K and Rb. *ACS Nano* **2011,** *5* (7), 5708-5716

(59) Chapman, J.; Su, Y.; Howard, C. A.; Kundys, D.; Grigorenko, A. N.; Guinea, F.; Geim, A. K.; Grigorieva, I. V.; Nair, R. R. Superconductivity in Ca-doped graphene laminates. *Sci Rep* **2016,** *6*, 23254

(60) Profeta, G.; Calandra, M.; Mauri, F. Phonon-mediated superconductivity in graphene by lithium deposition. *Nature Physics* **2012,** *8* (2), 131-134

(61) Inaba, M.; Yoshida, H.; Ogumi, Z.; Abe, T.; Mizutani, Y.; Asano, M. In Situ Raman Study on Electrochemical Li Intercalation into Graphite. *J. Electrochem. Soc.* **1995,** *142* (1), 20-26

(62) Zou, J.; Sole, C.; Drewett, N. E.; Velicky, M.; Hardwick, L. J. In Situ Study of Li Intercalation into Highly Crystalline Graphitic Flakes of Varying Thicknesses. *J Phys Chem Lett* **2016,** *7* (21), 4291-4296

(63) Zhao, W.; Tan, P. H.; Liu, J.; Ferrari, A. C. Intercalation of few-layer graphite flakes with FeCl3: Raman determination of Fermi level, layer by layer decoupling, and stability. *J Am Chem Soc* **2011,** *133* (15), 5941-5946

(64) Chacon-Torres, J. C.; Wirtz, L.; Pichler, T. Manifestation of charged and strained graphene layers in the Raman response of graphite intercalation compounds. *ACS Nano* **2013,** *7* (10), 9249-9259

(65) Gotoh, K.; Ueda, T.; Omi, H.; Eguchi, T.; Maeda, M.; Miyahara, M.; Nagai, A.; Ishida, H. Observation of micropores in hard-carbon using 129Xe NMR porosimetry. *Journal of Physics and Chemistry of Solids* **2008,** *69* (1), 147-152

(66) Bommier, C.; Ji, X.; Greaney, P. A. Electrochemical properties and theoretical capacity for sodium storage in hard carbon: Insights from first principles calculations. *Chemistry of Materials* **2018**, *31*(3), 658-677.